Journal of Materials Chemistry A

ROYAL SOCIETY OF CHEMISTRY

PAPER

View Article Online
View Journal | View Issue

Check for updates

Cite this: *J. Mater. Chem. A*, 2025, **13**, 14743

A nanocrystalline $La_{0.6}Sr_{0.4}Co_{0.4}Fe_{0.6}O_{3-\delta}$ interlayer for an enhanced oxygen electrode–electrolyte interface in solid oxide cells†

Juhwan Lee,[a] Kyoungjae Ju,[a] Ho Jun Yoo,[b] Sung Eun Jo,[a] Hyunmin Kim,[a] Geonwoo Park,[c] Geongu Han,[c] Woojin Park,[a] Gu Young Cho,[b] Hyong June Kim*[a] and Jihwan An*[ac]

A catalytically active and intimate interface between the electrode and electrolyte is crucial for the performance of solid oxide cells (SOCs). Here, we show that the nanocrystalline $La_{0.6}Sr_{0.4}Co_{0.4}Fe_{0.6}O_{3-\delta}$ (LSCF) functional interlayer fabricated by the sputtering process establishes an active and mechanically stable oxygen electrode/electrolyte interface and thereby reduces contact resistance with improving electrolysis cell (EC) durability. The LSCF interlayer with a thickness of over 100 nm enlarged the active electrochemical region, containing finely nanostructured grains and grain boundaries. This enhances ion transport and ionic charge transfer kinetics at the interface, resulting in threefold higher maximum power density in fuel cell (FC) mode and fourfold greater current density in EC mode compared with those in the reference cell at 650 °C. The EC durability test revealed a little cell voltage difference at 650 °C for 100 h. We clearly demonstrate that the precise control of the nanoscale morphology and crystallinity of the LSCF interlayer by thin-film deposition is important for developing high-performance thermally stable SOCs.

Received 10th February 2025
Accepted 2nd April 2025

DOI: 10.1039/d5ta01063b

rsc.li/materials-a

Jihwan An

Dr Jihwan An has been an associate professor in the Department of Mechanical Engineering and also an adjunct professor in the Graduate School of Semiconductor Technology and the Department of Battery Engineering at POSTECH, Korea, since 2023. Before joining POSTECH, he worked at SeoulTech, Korea (2014–2022). He received his PhD degree (2013) in Mechanical Engineering (major)/Materials Science (minor) from Stanford University. He is a member of the Young Korean Academy of Science and Technology (Y-KAST) and the recipient of the Top 10 Nanotechnologies award in 2023, awarded by the Ministry of Science and Technology, Korea. His research interests include interface and surface engineering of next-generation energy conversion and storage devices.

Introduction

Over the past two decades, the energy crisis and environmental pollution have accelerated global warming through greenhouse gas emissions, leading to climate change. Fossil fuels currently account for a major portion of our energy needs, but the CO, CO_2, SO_2, and many other toxins emitted from fossil fuels severely pollute the environment.[1,2] Recently, various energy devices have been developed to enhance the efficiency of batteries, capacitors, fuel cells, and water electrolysis, and they are expected to play a key role in the future energy industry.[3–7]

Solid oxide cells (SOCs) are electrochemical energy conversion devices attracting significant attention for overcoming the intermittency of renewable resources such as solar and wind power energy.[8–11] SOCs can reversibly operate in two modes with high efficiency: (i) the fuel cell (FC) mode to generate electrical energy from the chemical energy of fuels (*e.g.*, H_2 and CH_4) or (ii) the electrolysis cell (EC) mode to produce H_2 from electrical energy. However, the sluggish oxygen reduction reaction (ORR) and oxygen evolution reaction (OER) at the SOC electrode hinder the practical viability of SOC devices. Thus, the

[a]Department of Mechanical Engineering, Pohang University of Science and Technology (POSTECH), Pohang, Gyeongsangbuk-do 37673, Republic of Korea. E-mail: jihwanan@postech.ac.kr; hyongjunekim@postech.ac.kr

[b]Department of Mechanical Engineering, Dankook University, 152, Jukjeon-ro, Suji-gu, Yongin-si, Gyeonggi-do, 16890, Republic of Korea

[c]Department of Manufacturing Systems and Design Engineering, Seoul National University of Science and Technology (SeoulTech), Seoul 01811, Republic of Korea

† Electronic supplementary information (ESI) available. See DOI: https://doi.org/10.1039/d5ta01063b

development of SOC oxygen electrode materials and structural modifications are mandatory.

Currently, $La_xSr_{1-x}MnO_{3-\delta}$ (LSM), $La_xSr_{1-x}CoO_{3-\delta}$ (LSC), and $La_xSr_{1-x}Co_yFe_{1-y}O_{3-\delta}$ (LSCF) have been adopted as conventional SOC oxygen electrode materials due to their affordable electronic conductivity and catalytic activity. In particular, LSCF comprises superior *mixed ionic*-electronic conducting (MIEC) characteristics that can simultaneously transfer oxygen ions and electrons and lead to better thermochemical stability in contact with SOC electrolyte materials.[12,13] However, oxygen electrodes in SOCs inevitably undergo various thermal and chemical degradation phenomena. Several critical degradation issues were reported in SOCs, including Cr and sulfur poisoning of the oxygen electrode,[14,15] Sr segregation,[16,17] secondary phase formation between the oxygen electrode and the electrolyte,[18,19] and microstructural deformation.[20] Among these, the chemically and mechanically induced instability at the oxygen electrode/electrolyte interface is considered the most devastating issue because it can lead to complete cell failure in the entire SOEC system.[21] High-voltage, high-current, and long-term operation in EC mode can facilitate the formation of cracks, pores, and delamination along the oxygen electrode/electrolyte interface.[22] According to multiple studies on this delamination phenomenon, the prevailing hypothesis is that oxygen species generated by the OER become locally accumulated at the oxygen electrode/electrolyte interface, causing a buildup of oxygen gas pressure when gas migration or release through the oxygen electrode structure is hindered.[22–27]

Extensive research was conducted to address this issue by enhancing the OER kinetics through electrode surface coatings with catalytic materials[28,29] or by structural modifications, including the addition of porous electrolyte materials to promote oxygen gas release.[30–33] However, the application of catalytic materials does not directly address the underlying adhesion issues at the oxygen electrode/electrolyte interface, which can lead to inherent delamination under high-current conditions in SOECs. Furthermore, from a fundamental perspective, incorporating a porous electrolyte material at the interface can increase the ohmic resistance in proportion to the thickness of the added interlayer, which in turn may increase the overvoltage.[33] Thus, modifying the electrode surface and the electrode/electrolyte interface presents various practical challenges, highlighting the need for ongoing research on unresolved physical and chemical issues through the use of appropriate materials and optimized electrode designs.

To overcome these challenges and develop a durable oxygen electrode/electrolyte interface for SOCs, we employed a nanocrystalline LSCF functional interlayer deposited by sputtering at the oxygen electrode/electrolyte interface. The sputtering process induces strong adhesion of the film to the substrate due to the elevated thermal and kinetic energies during the process, with versatility in precisely controlling the composition (*e.g.*, alloys and multicomponent oxides) and microstructural features (*e.g.*, film thickness, grain size, and porosity).[34–40] We focused on structural modifications to enhance interfacial properties and clarify the relationship between the microstructure of the LSCF interlayer and the electrochemical performance of the cell. The SOC incorporating an LSCF interlayer (>100 nm) exhibits an approximately threefold (177 mW cm^{-2} *vs.* 544 mW cm^{-2}) and fourfold (93 mA cm^{-2} *vs.* 471 mA cm^{-2}) increase in maximum power density in FC mode and current density (at 1.3 V) in EC mode at 650 °C, respectively. Long-term stability testing in EC mode over 100 h at 650 °C and 250 mA cm^{-2} showed a threefold reduction in the degradation rate. This study provides a comprehensive insight into the rational design of functional interlayers at oxygen electrode/electrolyte interfaces to enhance the performance and durability of intermediate-temperature SOCs (IT-SOCs).

Experimental

Solid oxide cell fabrication

Solid oxide cells with a NiO–Y_2O_3 stabilized ZrO_2 (NiO–YSZ) fuel electrode|Y_2O_3 stabilized ZrO_2 (YSZ)|Sm_2O_3 doped CeO_2 (SDC)|LSCF interlayer|LSCF (oxygen electrode) configuration were fabricated using a commercialized anode-supported cell (1 × 1 cm^2, Kceracell), as illustrated in Fig. S1.† These anode-supported cells consisted of 650, 30, and 8 μm NiO–YSZ composite supports, a NiO–YSZ anode functional layer, and dense YSZ electrolyte, respectively. To avoid the formation of zirconates and improve the contact properties between the oxygen electrode and electrolyte,[41] a 700 nm samaria-doped ceria (SDC) electrolyte was deposited using radio-frequency (RF) sputtering with an SDC target (Sm 10 at%/Ce 90 at%, iTASCO) on top of the YSZ electrolyte. The working pressure was maintained at 3 mTorr at room temperature (RT). The sputtering power was 40 W at an Ar flow rate of 30 sccm. The LSCF interlayer was subsequently deposited on top of the SDC electrolyte. The samples were prepared with interlayer thicknesses of 0, 50, 100, 150, and 300 nm. The LSCF interlayer was deposited *via* RF sputtering from an LSCF target ($La_{0.6}Sr_{0.4}Co_{0.4}Fe_{0.6}O_{3-\delta}$, Advanced Engineering Materials Limited). The Ar plasma pressure in the sputtering chamber was 75 mTorr, and the deposition was performed at RT. The sputtering power was 40 W at an Ar flow rate of 30 sccm. The elemental compositions of the deposited LSCF interlayers are presented in Table S1.† On top of the LSCF interlayer, the LSCF oxygen electrode was deposited using a conventional screen-printing process. For the process, the LSCF slurry was first prepared by mixing LSCF powder (LSCF, Kceracell) with a binder (Kceracell), screen-printed, and sintered at 900 °C for 2 h.

Morphological and compositional analysis

The microstructures of the LSCF interlayers were investigated using field-emission scanning electron microscopy (FE-SEM, JSM-7800F Prime, JEOL) with energy-dispersive X-ray spectroscopy (EDS). The surface morphology was characterized using atomic force microscopy (AFM, Jupiter XR, Oxford Instruments). To evaluate the crystallinity of the LSCF interlayer, X-ray diffraction (XRD, Bruker DE/D8 Advance) with Cu Kα radiation was performed in 2θ scan mode. The samples were either used as-deposited or after annealing at 900 °C for 2 h on a Si (100) wafer. X-ray photoelectron spectroscopy (XPS, Nexsa) with a low-

power Al Kα X-ray source was used to examine the chemical composition of the LSCF interlayer. Prior to measurement, the sample underwent Ar etching at 1 keV for 30 s. The detachment experiment was conducted by applying a consistent 1.5 kg load to pull off the LSCF electrode under controlled measurement conditions across the entire cell area. The detached surface was subsequently examined by SEM-EDS.

Electrochemical analysis

For the cell test, an anode-supported cell (active area: 0.283 cm^2) was fixed onto a metal jig and sealed with sealing paste (Aremco). Porous Ni foam and Au mesh were used as current collectors for the fuel and oxygen electrodes, respectively, ensuring current collection. To enhance interface contact between the electrodes and collectors, a 1.5 kg load was applied during operation. The electrochemical performance of the cell was characterized using electrochemical impedance spectroscopy (EIS) and linear sweep voltammetry (LSV) with a potentiostat (Bio-Logic SP-300) in a customized probe station. EIS was performed at open circuit voltage (OCV) in the frequency range from 0.1 Hz to 1 MHz with a constant AC amplitude of 70 mV. The distribution of the relaxation time (DRT, DRTtools) was also used to characterize and deconvolute the EIS results related to multiple electrochemical reactions.[42] LSV was conducted by sweeping the voltage at a scan rate of 20 mV s^{-1}.

The cell performance was evaluated in both FC and EC modes at 600, 650, and 700 °C. For the FC test, dry H_2 was supplied to the NiO–YSZ fuel electrode at 150 sccm, whereas the LSCF oxygen electrode was provided with 150 sccm of dry air. For the EC operation, a 50 : 50 mixture of H_2 and H_2O, supplied with 150 sccm of dry H_2, was fed into the fuel electrode. The fuel composition was adjusted to achieve an OCV close to the Nernst potential.[43] This humidified fuel was directly supplied to the NiO–YSZ fuel electrode. For the LSCF oxygen electrode, 150 sccm of dry air was supplied to maintain a constant ambient air flow. The durability test was conducted in EC mode, and each sample was measured for approximately 100 h under the conditions of 650 °C and 250 mA cm^{-2}. For the current interruption test, a polarization current density of 250 mA cm^{-2} was applied for 30 s, after which the current was interrupted and the subsequent relaxation process was observed.

Results and discussion

Microstructure of the LSCF oxygen electrode interlayer

The change in the crystal structure of the LSCF interlayer was analysed using XRD (Fig. 1a). An amorphous LSCF interlayer with a thickness of approximately 200 nm was deposited by sputtering (blue areas in Fig. 1a). After annealing, distinct LSCF peaks were clearly observed (red parts in Fig. 1a, rhombohedral phase, JCPDS 48-0124), with no secondary phases. Using the Debye–Scherrer equation, the average grain size was determined to be 20.7 ± 2.8 nm, confirming the nanocrystalline nature of the annealed LSCF interlayer. XPS measurements were performed to further confirm the chemical composition of the as-deposited and annealed LSCF interlayer, and the results after

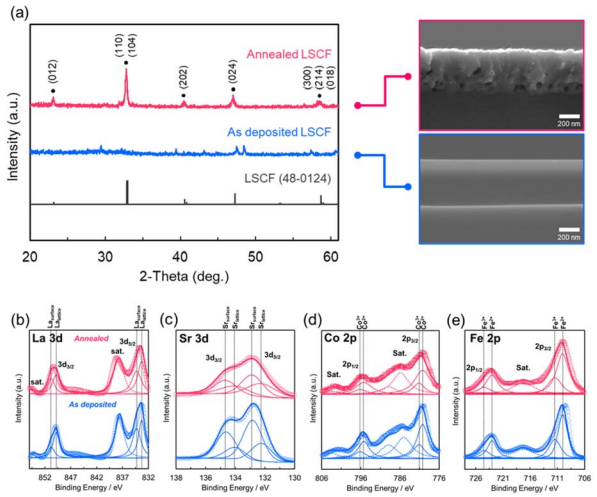

Fig. 1 (a) XRD survey spectra and cross-sectional SEM images and XPS spectra of (b) La 3d, (c) Sr 3d, (d) Co 2p, and (e) Fe 2p of the $La_{0.6}Sr_{0.4}Co_{0.4}Fe_{0.6}O_{3-\delta}$ (LSCF) interlayer, as deposited and annealed at 900 °C for 2 h on a Si (100) wafer.

Ar etching are shown in Fig. 1b–e and Table S1.† For the amorphous LSCF sample, the cation ratios of La, Sr, Co, and Fe were 30%, 19%, 19%, and 32%, respectively. After heat treatment, XPS results (Table S1†) confirmed that the composition of La, Sr, Co, and Fe remained largely unchanged compared to the as-deposited LSCF.

The surface morphologies of LSCF interlayers annealed at 900 °C as a function of film thickness (0–300 nm) were analysed using SEM and atomic force microscopy (Fig. 2). In the top-view SEM images, the as-deposited LSCF films show a morphology

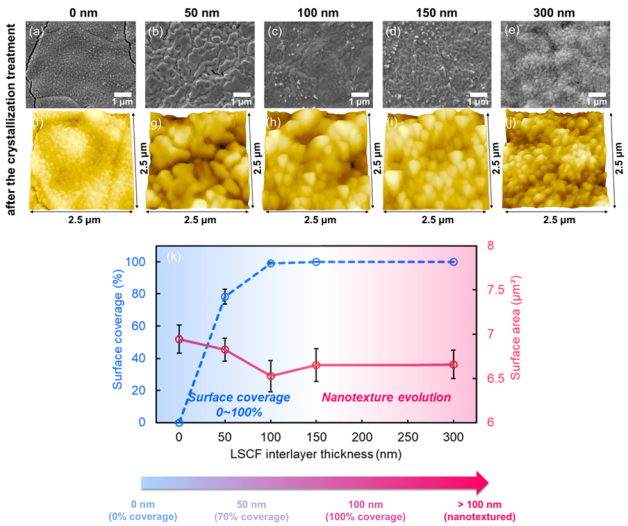

Fig. 2 Surface SEM and AFM images: (a and f) 0 nm, (b and g) 50 nm, (c and h) 100 nm, (d and i) 150 nm, and (e and j) 300 nm $La_{0.6}Sr_{0.4}Co_{0.4}Fe_{0.6}O_{3-\delta}$ (LSCF) interlayer. (k) Comparison of surface coverage and surface area as a function of LSCF interlayer thickness, demonstrating the morphological evolution of the LSCF interlayer on the samaria-doped ceria electrolyte sintered at 900 °C for 2 h (after heat treatment).

similar to that of the bare SDC layer surface regardless of the thickness, which is likely due to the amorphicity of the films (Fig. S2†). Upon annealing at 900 °C for 2 h, the 50 nm-thick LSCF layer is coarsened and pores are formed, partially covering the SDC layer with a surface coverage ratio of approximately 70% (Fig. 2b, g and S3†). When the thickness exceeds 100 nm, the LSCF interlayer continues to fully cover the SDC surface, exhibiting a nanocrystalline granular structure with an average grain size of approximately 200 nm, as shown in the surface images. Nanotextures also developed across the entire surface, accompanied by a slight increase in the surface area as the film thickness increased. For instance, at 2.5 × 2.5 μm^2, the measured surface areas are 6.53 and 6.66 μm^2 for the 100 nm and 300 nm samples, respectively (Fig. 2c–e and h–k).

Fig. 3 shows cross-sectional SEM images (with EDS mapping) of the LSCF oxygen electrode/LSCF interlayer/SDC electrolyte interfaces and their microstructural evolution upon annealing. In the 0 nm sample (Fig. 3a and f), a well-connected interface was scarcely formed, which limited the ion transfer between SDC and LSCF, leaving the SDC surface away from the LSCF–SDC interface inactive to the ORR/OER, which also implies the possible mechanical vulnerability of the interface at elevated temperatures. Contrastingly, samples with LSCF thicknesses greater than 50 nm (Fig. 3b–e and g–j) clearly show continuous LSCF oxygen electrode-LSCF interlayer-SDC channels (red circles in Fig. 3g–j), signifying the formation of facile ion transfer and transport pathways between the SDC electrolyte and LSCF oxygen electrode.[44] The primary reason for the formation of continuous interfaces is that the originally amorphous LSCF layer was oxidized upon annealing in air, which fostered oxidative interactions with adjacent LSCF electrodes.[45] From the perspective of solid–solid interactions, the mobility of small particles at elevated temperatures is easily driven by high thermal energy, promoting interfacial diffusion and strengthening bonding forces at the interfaces. In this context, the thermally active environment at 900 °C may have triggered the facile atomic movement of the amorphous LSCF layer with high surface energy and tightly integrated the LSCF oxygen electrode and interlayer. Additionally, the use of the same material between the electrode and interlayer may further enhance the tight integration *via* lattice matching.[46,47]

Simultaneously, high-temperature crystallization of the LSCF interlayer resulted in the formation of a nanocrystalline surface containing numerous grains and grain boundaries (Fig. S4†). On the LSCF interlayer surface, the OER/ORR occurs, where the fine nanostructure promotes ion transport and charge transfer through high-density grain boundaries.[48,49] This observation provides valuable insights into the influence of the nanocrystalline structure of the LSCF catalyst, further advancing our understanding of its catalytic roles.

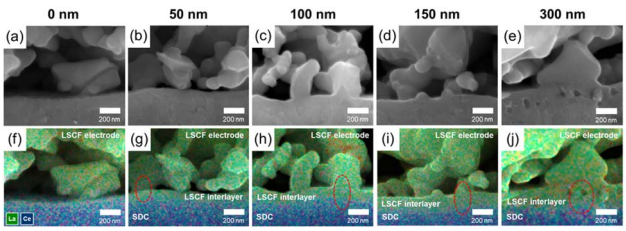

Fig. 3 Cross-sectional SEM images of the LSCF oxygen electrode/LSCF interlayer/SDC electrolyte interfaces with LSCF interlayer thickness variations: (a and f) 0 nm, (b and g) 50 nm, (c and h) 100 nm, (d and i) 150 nm, and (e and j) 300 nm.

Electrochemical performance in fuel cell mode

Fig. 4 shows the electrochemical performance of the NiO–YSZ supported full cell in the H_2–air FC mode as a function of the LSCF interlayer thickness. Both the *I–V–P* curve and EIS measurements were performed at an operating temperature of 650 °C; the electrochemical data at various temperatures (600, 650, and 700 °C) are shown in Fig. S5.† The open-circuit voltage (OCV) was maintained at 1.1 V, close to the Nernst potential. The *I–V–P* curves at 650 °C of reference, 50, 100, 150, 300 nm samples are shown in Fig. 4a, corresponding to a maximum power density (P_{max}) of 177, 341, 500, 540, and 544 mW cm^{-2}, respectively; the cell performance was almost saturated at the thickness of 100 nm, and slightly increased as the thickness further increases. The SOFC with the LSCF interlayer was also evaluated using EIS analysis. In the Nyquist plot obtained at OCV and at 650 °C (Fig. 4b and c), the ohmic resistance (R_o) was 0.43 Ω cm^2 in the reference, and slightly decreased to 0.16–0.21 Ω cm^2 at all thicknesses due to the improved contact between

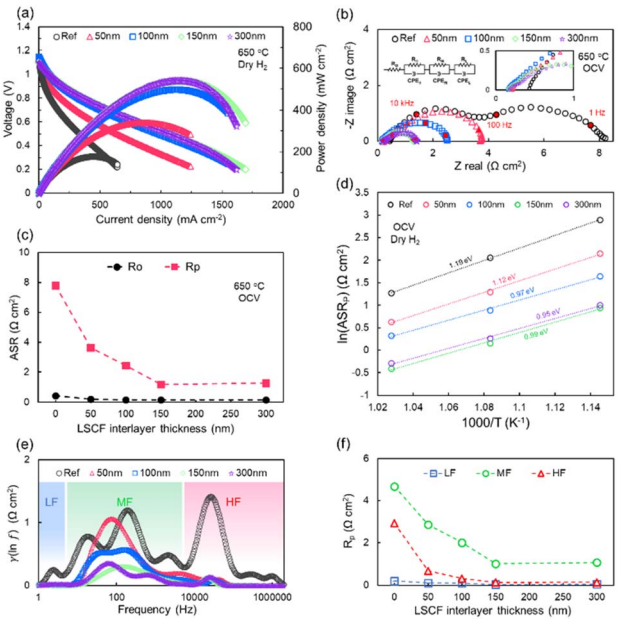

Fig. 4 Electrochemical performances of the SOFC with the reference sample and $La_{0.6}Sr_{0.4}Co_{0.4}Fe_{0.6}O_{3-\delta}$ (LSCF) interlayered samples evaluated at 650 °C with dry H_2 in the Ni-YSZ fuel electrode and dry air in the LSCF oxygen electrode: (a) *I–V–P* plots, (b) comparison of impedance spectra with those of Nyquist plots, (c) ohmic and polarization resistances, (d) Arrhenius plots for R_p in the temperature range from 600–700 °C under OCV and (e) distribution of the relaxation time plots, and (f) R_p values at LFs, MFs, and HFs for all prepared samples as a function of LSCF interlayer thickness.

the electrode and electrolyte; the polarization resistance (R_p) decreased from 7.78 Ω cm^2 in the reference and saturated at 1.26 Ω cm^2 in the >150 nm sample. Fig. 4d further presents the Arrhenius plots for R_p at temperatures between 600 and 700 °C. Compared with that of the activation energy of the reference sample (1.19 eV), a gradual decrease in the activation energy was observed as the LSCF interlayer became thicker: 50 nm (1.12 eV), 100 nm (0.97 eV), 150 nm (0.99 eV), and 300 nm (0.95 eV). The DRT was further investigated for a more in-depth analysis of the origin of the polarization resistance (Fig. 4e). Based on previous reports, the DRT plots were divided into three electrochemical processes: high- (HF), medium- (MF), and low-(LF) frequencies. The HF range (>10^4 Hz) is related to oxygen ion transport in the MIEC network and ion transfer at the oxygen electrode–electrolyte interface, the MF range (10^1 to 10^4 Hz) includes the effect of oxygen surface exchange and oxygen reduction (in FC)/evolution (in EC) reactions on the oxygen electrode surface, and the LF range (<10^1 Hz) is related to oxygen gas diffusion in the pores of the oxygen electrode.[50,51] To quantitatively analyse the DRT peak distribution, the areal ratio of the DRT peaks and the values of the total R_p were utilized, and the values of R_{HF}, R_{MF}, and R_{LF} in each frequency range were calculated (Fig. 4f). Overall, the R_p resistance was distributed in the order of $R_{MF} > R_{HF} > R_{LF}$, with R_{MF} and R_{HF} making the dominant contributions, *i.e.*, more than 90% of total R_p, which is consistent with that of the findings of an earlier study.[52] The peaks related to R_{HF}, R_{MF}, and R_{LF} showed a tendency to decrease with increasing thickness; R_{MF} was 4.67, 2.86, 2.02, 1.02 and 1.08 Ω cm^2, and R_{HF} was 2.91, 0.67, 0.32, 0.12, and 0.14 Ω cm^2 in the reference, 50, 100, 150, and 300 nm samples, respectively, as summarized in Table S2.† The decrease in resistance corresponding to these HF and MF signals can be attributed to the enhancement of ionic charge transfer kinetics triggered by the expansion of the heterogeneous interfaces between the LSCF interlayer and SDC and the increase in active surface area with the facilitated catalytic reaction resulting from the numerous grain boundaries near the LSCF surface. The resistance to gas diffusion in the oxygen electrodes was almost negligible, as confirmed by the absence of the R_{LF}.

Electrochemical performance in electrolysis cell mode

Fig. 5 shows the electrochemical performance of the NiO–YSZ-supported full cell in the EC mode with varying LSCF interlayer thicknesses. A humidified gas containing 50% H_2 and 50% H_2O was supplied to the fuel electrode, and dry air was delivered to the oxygen electrode. Fig. 5a shows that the OCV is approximately 0.95 V under the corresponding humidified conditions, which is close to that of the Nernst potential (~1 V) at 650 °C by supplying 50 : 50 H_2/H_2O.[53,54] For evaluation of *I*–*V* curves in EC operation, the current densities at 1.3 V, which is close to that of the thermoneutral voltage of 1.29 V, and the relatively high voltage of 1.6 V, are summarized in Fig. S6.† At 1.3 V, reference, 50, 100, 150, and 300 nm samples showed current densities of 93, 330, 456, 471, and 428 mA cm^{-2}, respectively. Similar to that of the FC mode results, no significant change was observed in

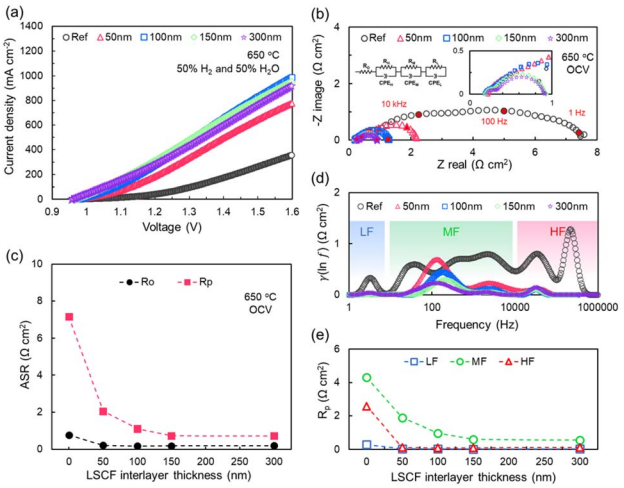

Fig. 5 Electrochemical performances of the SOEC with the reference sample and LSCF interlayered samples evaluated at 650 °C with dry H_2 and H_2O (50 : 50) in the fuel electrode and dry air in the LSCF oxygen electrode: (a) *I*–*V* plots, (b) comparison of impedance spectra with Nyquist plots, (c) ohmic and polarization resistances, (d) DRT plots, and (e) R_p values at high- (HF), medium- (MF), and low-(LF) frequencies for all prepared samples as a function of LSCF interlayer thickness.

the thickness range of >100 nm, with a marginal decrease in the 300 nm sample. Compared with that of the reference, the current densities were 4 times larger in the 100 nm sample. EIS was conducted, as shown in Fig. 5b and c. The Nyquist plots extracted from the EIS spectra showed ohmic resistances (R_o) of 0.77, 0.21, 0.18, 0.19, and 0.20 Ω cm^2. The polarization resistances (R_p) were 7.16, 2.05, 1.11, 0.73, and 0.73 Ω cm^2, which demonstrate that the reduction in R_p was a dominant factor in the increased current density. Additionally, using DRT analysis, R_p was deconvoluted into several peaks (Fig. 5d and e). Similar to those in the FC mode, R_{MF} and R_{HF} sharply dropped from 4.30 and 2.57 Ω cm^2 in the reference to 0.61 and 0.10 Ω cm^2 in the 150 nm sample, and thereafter saturated (Table S3†).

Durability test in electrolysis cell mode

Prominently, SOECs suffer from mechanical degradation such as pores, cracks, and delamination at the oxygen electrode–electrolyte interface.[55] Therefore, we investigated the impact of the LSCF interlayer on the durability of the cells: the reference *vs.* the cell with the 100 nm LSCF interlayer at 650 °C, 250 mA cm^{-2} for 100 h (Fig. 6a). The performance of the reference sample clearly showed a significant decrease over time; the voltage increases from 1.4–1.6 V after 80 h. Contrastingly, the voltage of the 100 nm sample started at 1.2 V and only increased by about 0.06 V after 100 h of operation. In EIS analysis (Fig. S7†), the ohmic resistance of the reference sample showed a linear increase of about 54% from 0.49–0.75 Ω cm^2 during 100 h. This increase in the ohmic resistance seems to be due to a structural defect occurring at the oxygen electrode–electrolyte interface, which is mainly caused by the accumulation of oxygen species resulting from the OER at the oxygen electrode and electrolyte interface during EC operation.[55] In the case of the

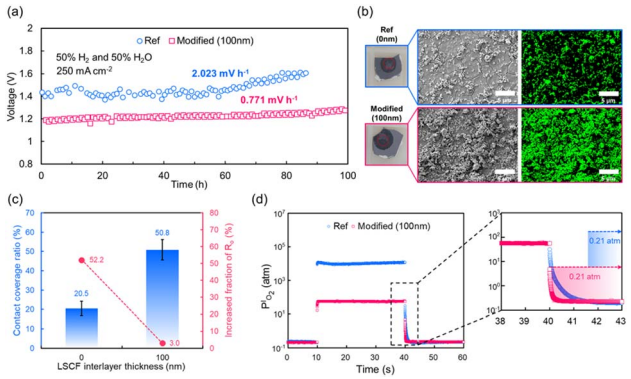

Fig. 6 (a) Long-term durability test for comparison of stability of reference and modified samples at 650 °C, 250 mA cm^{-2} for 100 h in EC mode. (b) Scanning electron microscopy images after the detachment experiment with SOCs long-term operated and (c) comparison between the contact coverage ratio and increased fraction of R_O. (d) The change of the oxygen partial pressure at the LSCF oxygen electrode/SDC electrolyte interface for reference and modified samples in the current interruption experiment conducted at an operating temperature and current density of 650 °C and 250 mA cm^{-2}, respectively.

modified samples, little difference was observed in ohmic resistance (0.15 Ω cm^2) possibly due to the improved interfacial stability. Fig. S8† illustrates the structural differences observed in the reference and modified samples before and after 100 h of electrochemical operation, indicating that the LSCF interlayer effectively suppressed the formation of interfacial defects. The preservation of the intimate interface by stronger adhesion was also clearly shown in the electrode detachment test after the operation (Fig. 6b and c). The surface coverage ratio of the remaining LSCF electrode was 20.5 ± 3.7% in the reference and 50.8 ± 5.3% in the 100 nm sample. Indeed, in previous studies on the adhesion strength at these interfaces,[56,57] it was shown that such a high contact coverage on the surface of the electrolyte causes an increase in the tensile strength at the electrode/electrolyte interface, thereby reinforcing the wettability and cell durability, which is the case for the oxygen electrode interface of the LSCF-interlayered cell in our experiment.

Additionally, we characterized the release of oxygen species at the oxygen electrode–electrolyte interface using the current interruption method (Fig. 6d). Mechanical issues at the oxygen electrode–electrolyte interface of SOECs are known to be mainly due to the oxygen gas species formed by the OER not being rapidly released from the oxygen electrode and accumulating at the interface, which causes significant stress. In particular, electrolyte surfaces are known to exhibit critical mechanical defects when not combined with electrodes, likely due to the restricted release of oxygen species along electrochemically inactive surfaces.[58] It is understood that the relaxation rate at which the oxygen pressure on the oxygen electrode side reaches 0.21 atm right after a current interruption is related to the extent of oxygen species release from the interface.[59,60] Here, a polarization current density of 250 mA cm^{-2} was applied for about 30 s, and a relaxation process was observed after the current was interrupted (Table S4†). As a result, once the current flow was interrupted, the interfacial oxygen partial pressure of the reference sample was found to saturate at 0.21 atm after about 2 s, whereas in the modified (100 nm) sample, the pressure reached 0.21 atm within only 0.2 s, showing a much steeper gradient. These findings suggest that the enlarged electrochemical region at the interface allowed the OER to occur in a broader interfacial region rather than in a localized region, such as around the LSCF electrode particles, which facilitated the diffusion of oxygen gas species in the closed pores or cavities present at the interface into the air.

Furthermore, to support the proposed mechanism of mechanical defects at the interface, we analysed compositional changes caused by differences in oxygen potential before and after EC operation (Fig. S9†). Linear intensity profiles of Ce, Sm, and O were measured across the SDC electrolyte region. For the reference sample, the oxygen intensity increased near the SDC surface (<200 nm), which implies the accumulation of oxygen at the SDC–LSCF interface. In contrast, the modified sample exhibited negligible compositional changes both at the surface and within the bulk of SDC. These results strongly suggest that the LSCF interlayer effectively suppressed oxygen accumulation at the interface due to facilitated oxygen ion transfer.

In summary, the LSCF interlayered SOC showed improved cell performance and durability (Fig. 7a). Fig. 7b and c represent possible mechanisms in multiple aspects for our results:

(i) Electrochemical performance: the enlarged heterogeneous interfaces between the LSCF interlayer and SDC may have facilitated ionic transfer by offering more pathways compared to the reference cell for oxygen ion movement across the interfaces (yellow arrows in Fig. 7b and c). Furthermore, high-density grain boundaries of the LSCF interlayer may have expedited the oxygen ion transport across the interlayer (blue

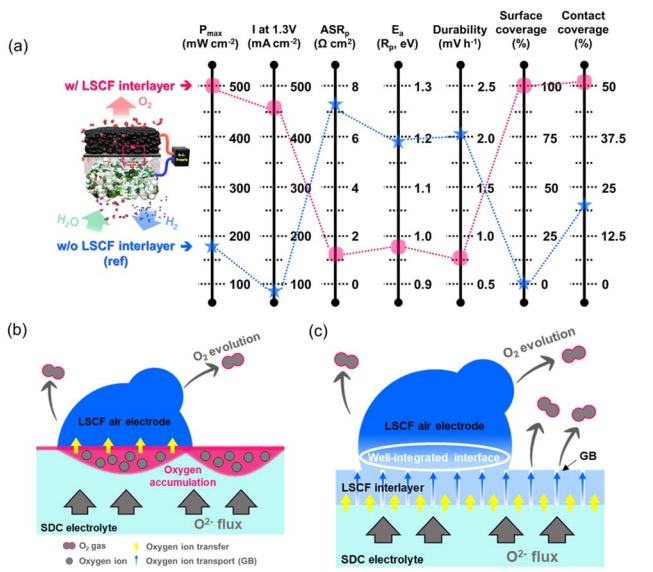

Fig. 7 (a) Comparison of the structural characteristics and electrochemical performances. Schematic illustrations of the proposed reaction mechanisms: (b) reference (w/o the LSCF interlayer) and (c) modified (w/o the LSCF interlayer) samples.

arrows in Fig. 7b and c).[48,49] The enlargement of the LSCF surface with nano-grains also promoted the surface exchange and charge transfer reactions, which are the rate-limiting steps in the overall ORR/OER process.[61]

(ii) Stability: the facilitated oxygen evolution at the LSCF surface may have suppressed oxygen ion species buildup at the LSCF/SDC interface (red region in Fig. 7b), which is one of the main reasons for mechanical degradation in SOECs.[55] The tight integration between the LSCF oxygen electrode and interlayer after annealing is also beneficial for thermal stability (white circle in Fig. 7c).

As a result, the combined effects of the mechanisms above seem to have contributed to the high performance and stable operation of nanocrystalline LSCF-interlayered SOECs.

Conclusion

Here, we proposed a novel strategy to boost the performance and enhance EC durability by adding a nanocrystalline LSCF interlayer at the oxygen electrode/electrolyte interface through sputtering deposition. The LSCF interlayered SOC (>100 nm) showed a high peak power density threefold higher at 650 °C under FC operation and a current density more than fourfold higher under EC operation (at 1.3 V). The EIS and DRT data revealed that the reduction in cell resistance was mainly due to a decrease in the polarization resistance. These performance improvements are attributed to the enlarged electrochemically active area, heterogeneous junctions at the interfaces, and oxidative interactions at the LSCF oxygen electrode/LSCF interlayer/SDC electrolyte interfaces. The EC mode operation for approximately 100 h demonstrated that the LSCF interlayer also mitigated EC delamination, thereby improving the SOC durability.

Data availability

All data supporting this research are included in the main article and the ESI.†

Author contributions

Juhwan Lee: conceptualization, formal analysis, investigation, writing – original draft. Kyoungjae Ju: methodology, investigation. Ho Jun Yoo: methodology, investigation. Sung Eun Jo: methodology. Hyunmin Kim: validation, writing – review & editing. Geonwoo Park: methodology. Geongu Han: methodology. Woojin Park: methodology. Gu Young Cho: methodology, validation. Hyong June Kim: conceptualization, supervision, writing – review & editing. Jihwan An: conceptualization, supervision, writing – review & editing.

Conflicts of interest

No conflicts of interest have been declared.

Acknowledgements

This research was supported by the Basic Science Research Program through the National Research Foundation of Korea (NRF) funded by the Ministry of Education (NRF-2021R1A6A1A03039981), the National Research Foundation of Korea (NRF) grant funded by the Korea government (MSIT) (No. 2022R1A2C4001205) and, Korea Institute of Energy Technology Evaluation and Planning (KETEP) grant funded by the Korea government (MOTIE) (No. 20213030030040).

References

1 B. C. Steele and A. Heinzel, *Nature*, 2001, **414**, 345–352.
2 J. A. Turner, *Science*, 2004, **305**, 972–974.
3 F. Liu, X. Lu, C. Shi and Z. Sun, *Batter. Supercaps*, 2024, **7**, e202481102.
4 J. Sun, L. Miao, Z. J. Xu and Z. Sun, *Inorg. Chem. Front.*, 2025, **12**, 2417–2425.
5 X. Xu, S. Zhang, Q. Zhang, S. Chen, Y. Wu and Z. Sun, *ACS Sustainable Chem. Eng.*, 2023, **11**, 15338–15349.
6 R. Wang, Y. Yang, X. Xu, S. Chen, A. Trukhanov, R. Wang, L. Shao, X. Lu, H. Pan and Z. Sun, *Inorg. Chem. Front.*, 2023, **10**, 1348–1356.
7 X. Xu, H. Liao, L. Huang, S. Chen, R. Wang, S. Wu, Y. Wu, Z. Sun and H. Huang, *Appl. Catal., B*, 2024, **341**, 123312.
8 A. Hauch, R. Küngas, P. Blennow, A. B. Hansen, J. B. Hansen, B. V. Mathiesen and M. B. Mogensen, *Science*, 2020, **370**, eaba6118.
9 M. B. Mogensen, M. Chen, H. L. Frandsen, C. Graves, J. B. Hansen, K. V. Hansen, A. Hauch, T. Jacobsen, S. H. Jensen, T. L. Skafte and X. Sun, *Clean Energy*, 2019, **3**, 175–201.
10 H. Kim, C. Lim, J. Gu, H. Y. Jeong, J. W. Han, J. H. Jang and Y. Bu, *Adv. Energy Mater.*, 2024, **14**, 2401307.
11 H. Liu, L. R. Clausen, L. Wang and M. Chen, *Energy Environ. Sci.*, 2023, **16**, 2090–2111.
12 Y. Lim, J. Park, H. Lee, M. Ku and Y.-B. Kim, *Nano Energy*, 2021, **90**, 106524.
13 J. Zhang, S. Ricote, P. V. Hendriksen and Y. Chen, *Adv. Funct. Mater.*, 2022, **32**, 2111205.
14 N. Ni, C. C. Wnag, S. P. Jiang and S. J. Skinner, *J. Mater. Chem. A*, 2019, **7**, 9253–9262.
15 J. A. Schuler, H. Yokokawa, C. F. Calderone, Q. Jeangros, Z. Wuillemin, A. Hessler-Wyser and J. V. Herle, *J. Power Sources*, 2012, **201**, 112–120.
16 B. Koo, K. Kim, J. K. Kim, H. Kwon, J. W. Han and W. Jung, *Joule*, 2018, **2**, 1476–1499.
17 W. Jung and H. L. Tuller, *Energy Environ. Sci.*, 2012, **5**, 5370–5378.
18 M. Z. Khan, R.-H. Song, M. T. Mehran, S.-B. Lee and T.-H. Lim, *Ceram. Int.*, 2021, **47**, 5839–5869.
19 J. S. Hardy, C. A. Coyle, J. F. Bonnett, J. W. Templeton, N. L. Canfield, D. J. Edwards, S. M. Mahserejian, L. Ge, B. J. Ingram and J. W. Stevenson, *J. Mater. Chem. A*, 2018, **6**, 1787–1801.

20 A. Mahata, P. Datta and R. N. Basu, *J. Alloys Compd.*, 2015, **627**, 244–250.
21 A. Nechache and S. Hody, *Renew. Sustain. Energy Rev.*, 2021, **149**, 111322.
22 Z. Pan, Q. Liu, Z. Yan, Z. Jiao, L. Bi, S. H. Chan and Z. Zhong, *Electrochem. Commun.*, 2022, **137**, 107267.
23 A. V. Virkar, *Int. J. Hydrogen Energy*, 2010, **35**, 9527–9543.
24 M. Nerat and Đ. Juričić, *Int. J. Hydrogen Energy*, 2018, **43**, 8179–8189.
25 Y. Wen and K. Huang, *J. Electrochem. Soc.*, 2024, **171**, 034510.
26 L. Wu, H. Zheng, X. Yang, H. Qi, B. Tu, C. Zang, L. Jia and P. Qiu, *ACS Appl. Mater. Interfaces*, 2023, **15**, 52673–52685.
27 M. Krammer, A. Schmid, M. Siebenhofer, A. E. Bumberger, C. Herzig, A. Limbeck, M. Kubicek and J. Fleig, *ACS Appl. Energy Mater.*, 2022, **5**, 8324–8335.
28 S. U. Rehman, S. Qamar, M. H. Hassan, H.-S. Kim, R.-H. Song, T.-H. Lim, J.-E. Hong, S.-J. Park, D.-W. Joh and S.-B. Lee, *J. Eur. Ceram. Soc.*, 2023, **43**, 1559–1566.
29 H. Fan and M. Han, *Faraday Discuss.*, 2015, **182**, 477–491.
30 N. Li, M. Keane, M. K. Mahapatra and P. Singh, *Int. J. Hydrogen Energy*, 2013, **38**, 6298–6303.
31 X. Wang, B. Yu, W. Zhang, J. Chen, X. Luo and K. Stephan, *Int. J. Hydrogen Energy*, 2012, **37**, 12833–12838.
32 M. S. Khan, X. Xu, R. Knibbe and Z. Zhu, *ACS Appl. Mater. Interfaces*, 2018, **10**, 25295–25302.
33 M. S. Khan, X. Xu, J. Zhao, R. Knibbe and Z. Zhu, *J. Power Sources*, 2017, **359**, 104–110.
34 Y. H. Lee, H. Ren, E. A. Wu, E. E. Fullerton, Y. S. Meng and N. Q. Minh, *Nano Lett.*, 2020, **20**, 2943–2949.
35 H. Ren, Y. H. Lee, E. A. Wu, H. Chung, Y. S. Meng, E. E. Fullerton and N. Q. Minh, *ACS Appl. Energy Mater.*, 2020, **3**, 8135–8142.
36 A. A. Solovyev, K. A. Kuterbekov, S. A. Nurkenov, A. S. Nygymanova, A. V. Shipilova, E. A. Smolyanskiy, S. V. Rabotkin and I. V. Ionov, *Fuel Cells*, 2021, **21**, 408–412.
37 A. Solovyev, A. Shipilova, S. Rabotkin, E. Smolyanskiy and A. Shmakov, *Int. J. Hydrogen Energy*, 2022, **47**, 37967–37977.
38 K. Akimoto, N. Wang, C. Tang, K. Shuto, S. Jeong, S. Kitano, H. Habazaki and Y. Aoki, *ACS Appl. Energy Mater.*, 2022, **5**, 12227–12238.
39 E. A. Smolyanskiy, S. A. Linnik, I. V. Ionov, A. V. Shipilova, V. A. Semenov, A. L. Lauk and A. A. Solovyev, *J. Phys. Conf. Ser.*, 2018, **1115**, 032080.
40 D. Jeong, G. Jang and S. Hong, *Nanomaterials*, 2024, **14**, 561.
41 Q. Lyu, H. Zhao, J. He, Y. Wang, Y. Xiang, H. Qu, Q. Zhong, Y. Sun and T. Zhu, *J. Mater. Chem. A*, 2024, **12**, 9778–9786.
42 T. H. Wan, M. Saccoccio, C. Chen and F. Ciucci, *Electrochim. Acta*, 2015, **184**, 483–499.
43 K. Develos-Bagarinao, T. Ishiyama, H. Kishimoto, H. Shimada and K. Yamaji, *Nat. Commun.*, 2021, **12**, 3979.
44 K. Develos-Bagarinao, J. D. Vero, H. Kishimoto, T. Ishiyama, K. Yamaji, T. Horita and H. Yokokawa, *Nano Energy*, 2018, **52**, 369–380.
45 J. N. Israelachvili, *Intermolecular and Surface Forces*, Academic press, 2011.
46 L. Treccani, *Surface-Functionalized Ceramics: For Biotechnological and Environmental Applications*, 2023, pp. 47–84.
47 J. Cao, Y. Li, Y. Zheng, S. Wang, W. Zhang, X. Qin, G. Geng and B. Yu, *Adv. Energy Mater.*, 2022, **12**, 2200899.
48 X. Geng, M. Vega-Paredes, Z. Wang, C. Ophus, P. Lu, Y. Ma, S. Zhang, C. Scheu, C. H. Liebscher and B. Gault, *Nat. Commun.*, 2024, **15**, 8534.
49 R. Chattot, O. Le Bacq, V. Beermann, S. Kühl, J. Herranz, S. Henning, L. Kühn, T. Asset, L. Guétaz, G. Renou, J. Drnec, P. Bordet, A. Pasturel, A. Eychmuller, T. J. Schmidt, P. Strasser, L. Dubau and F. Maillard, *Nat. Mater.*, 2018, **17**, 827–833.
50 M. Ghamarinia, A. Babaei, C. Zamani and H. Aslannejad, *Chem. Eng. J. Adv.*, 2023, **15**, 100503.
51 H. Sumi, H. Shimada, Y. Yamaguchi, T. Yamaguchi and Y. Fujishiro, *Electrochim. Acta*, 2020, **339**, 135913.
52 J. Lee, S. Hwang, M. Ahn, M. Choi, S. Han, D. Byun and W. Lee, *J. Mater. Chem. A*, 2019, **7**, 21120–21127.
53 H. Li, H. J. Kim, T. Garcia, G. Park, Y. Ding, M. Liu, J. An and M. H. Lee, *ACS Catal.*, 2023, **13**, 11172–11181.
54 P. Li, Y. Han, M. Xu, T. Jin, F. Yan, T. Gan and R. Wang, *Energy Fuels*, 2022, **36**, 15165–15176.
55 M. Khan, X. Xu, R. Knibbe and Z. Zhu, *Renew. Sustain. Energy Rev.*, 2021, **143**, 110918.
56 H. S. Yoo, S. J. Kim, Y. T. Megra, J. Lee, J. W. Suk and W. Lee, *Appl. Surf. Sci.*, 2023, **639**, 158188.
57 N. Hildenbrand, B. A. Boukamp, P. Nammensma and D. H. Blank, *Solid State Ionics*, 2011, **192**, 12–15.
58 H. Choi, J. Shin, C. Yeon, S.-Y. Park, S.-T. Bae, J. W. Kim, J.-H. Lee, J.-W. Park, C.-W. Lee and K. J. Yoon, *Energy Environ. Sci.*, 2024, **17**, 5410–5420.
59 H. Dai, S. He, H. Chen, S. Yu and L. Guo, *J. Power Sources*, 2015, **280**, 406–409.
60 C. Su, Z. Lü, C. Wang, J. Li, P. Li, X. Yue and H. Li, *Int. J. Hydrogen Energy*, 2019, **44**, 14493–14499.
61 C. Li, X. Tong, C. Yuan, Y. Tong, Y. Zhang, N. Wang, P. Li, S. Pang, L. Wang and Z. Zhan, *Ceram. Int.*, 2024, **50**, 4656–4664.

